In-situ SEM characterization and numerical modelling of bainite formation and impingement of a medium- carbon, low-alloy steel

O. Seppälä [a,*], A. Pohjonen [a], J. Mendonça [b,c], V. Javaheri [a], R. Podor [b], H. Singh [d], J. Larkiola [a]

[a] Materials and Mechanical Engineering, University of Oulu, Oulu 90014, Finland
[b] ICSM, Univ Montpellier, CNRS, CEA, ENSCM, Marcoule, France
[c] NewTEC Scientific, Caveirac, France
[d] Nano and Molecular Systems Research Unit, University of Oulu, Oulu 90014, Finland

HIGHLIGHTS

- A novel in-situ SEM method was used to observe bainite formation in a medium carbon steel, and the results corresponded well to dilatometer and ex-situ SEM-EBSD results.
- Thermal cycle was designed using a previously developed mean field model, succesfully producing a suitable austenitic grain structure and cooling to bainite formation temperature.
- A Cellular Automata (CA) model was applied to reproduce the dynamical nucleation, growth and inpingement phenomena of the bainite regions. The model was parameterized by utilizing experimental data.
- CA model was enhanced by reworking the rate parameter equation and statistical accuracy was increased with multiple repetitions.

GRAPHICAL ABSTRACT
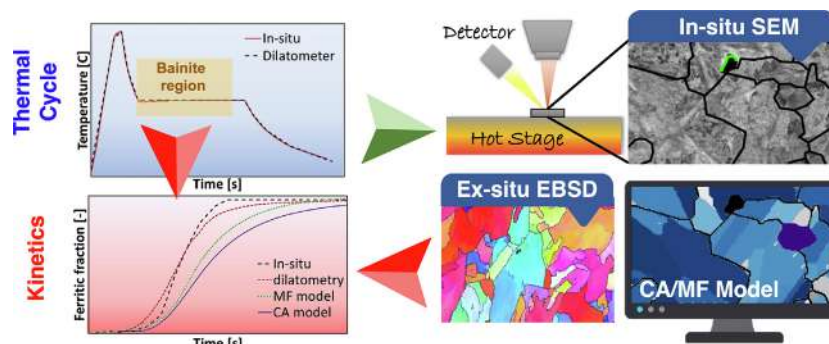
ARTICLE INFO

ABSTRACT

A novel in-situ scanning electron microscope (SEM) characterization technique for observing phase transformation is developed and its results studied and compared to well-founded experimental ex-situ methods as well as numerical modelling of bainite formation. Phase transformation kinetics are compared between the in-situ SEM, dilatometry test as well as mean field and Cellular Automata (CA) models. Microstructural evolution during phase transformation is compared between in-situ SEM, ex-situ EBSD and CA model results. The in-situ method allows for direct observation of bainite sheaf growth and impingement. The in-situ results in combination with EBSD data can be used to parameterize the CA model sheaf nucleation and growth equations.

© 2023 The Author(s). Published by Elsevier Ltd. This is an open access article under the CC BY-NC-ND license (http://creativecommons.org/licenses/by-nc-nd/4.0/).

---

* Corresponding author.
  E-mail address: oskari.seppala@oulu.fi (O. Seppälä).

1. Introduction

Development of steel must evolve constantly to keep up with the high demands of steel industry. Because microstructure has a decisive influence on the mechanical properties of steel, it is of paramount importance to understand the evolution of microstructure during thermal processing. As the modern steel concepts increase in complexity, traditional research methods may not be able to produce sufficiently in-depth information about the relevant phenomena. In such a case, new methods should be sought to see more than before, unencumbered by the limits of the old ways. The ultimate goal for steel microstructure modelling is to obtain a quantitative predictive model, which can describe the essential features of the microstructure formation, in particular at high temperature. Such a model would then allow virtual experimentation for microstructural design. As a step toward this goal, this work aims to quantify the shape-defining parameters of the previously developed cellular automata model [1], based on in-situ microscopy hot-stage SEM experiments [2–4] and ex-situ EBSD analysis.

Due to the apparent technological importance of controlling the microstructure evolution by the cooling process parameters, numerical modeling of phase transformations has been a subject of numerous earlier studies. An overview of different methodologies used for simulating phase transformations in steels is given in [5]. Here, we mention some examples of usage of similar models from different decades.

Umemoto et al. simulated pearlite formation during continuous cooling assuming additivity and Kolmogorov-Johnson-Mehl-Avrami (KJMA) equation [6]. The phase transformation model that had been fitted to several different steel compositions was described in [7]. Comprehensive modeling of different aspects of microstructure development in steels was examined in [8], including austenite decomposition and ferrite grain size. Serajzadeh modeled phase transformations and heat condution in hot-strip runout table cooling conditions [9]. Hot deformation and phase transformation phenomena were modeled in [10], where also usage of cellular automata models were described. Chen constructed a coupled phase transformation heat conduction simulation for Jominy end quench test [11]. Chen et al. applied a generalized additivity rule for simulating the phase transformations during cooling [12]. More recently Zhao et al. applied KJMA and Kamamoto equations for modeling the phase transformations with a coupled finite element heat conduction model using Abaqus software to simulate hot stamping process [13].

We have previously developed a coupled heat conduction and mean field (MF) phase transformation model [14–17], that has been applied for simulating austenite decomposition in cooling of a steel coil [15] as well as in slow cooling of low temperature ausformed steel, which leads to the formation of fine bainitic structure [18]. The mean field phase transformation model has been also used for simulating microstructure evolution to aid the design of induction hardening of a medium carbon pipeline material [19] where the model can be used for optimizing the cooling path and strategy so that desired fractions of different phases can be obtained [20,21] through the pipe thickness. Using this model, it is possible to quantitatively estimate the phase fraction and final hardness. In the current study, the mean field model is used to predict phase transformation process and design the thermal cycle to produce bainitic microstructure.

To simulate the approximate morphology of microstructure formation, we have earlier developed a two dimensional cellular automata (CA) model [1] which calculates the nucleation, growth, and impingement of bainite sheaves [22]. The temperature depen-dent rate parameter obtained from the parameterized mean field model is used as input for the CA model. The ratio of nucleation to growth and the aspect ratio of the growing bainite regions are determined from the observed microstructure.

In other studies, CA has been implemented in various ways to study the microstructural evolution of steel. In [23], several continuous cooling paths were used to simulate growth of ferritic phases as well as carbon diffusion in a complex phase steel. In [24], the full annealing cycle of a dual phase steel was simulated with a 3D CA model. A CA model was combined with a finite element model in [25] to simulate cold rolling on the microstructure and to simulate the subsequent annealing. Elahi et al. [26] compared phase-field and CA models to simulate the grain growth competition during melt pool solidification.

The formation of bainite can be observed on the surface, due to the surface relief which is created by the shear displacements [27]. Nucleation and growth of bainite have been previously examined with in-situ measurements using a laser scanning confocal microscope [28,29]. Advanced microscopy has been used in other studies to observe steel microstructure. Heard et al. [30] showed the possibility and challenges of high temperature in-situ SEM to observe and to document the phase transformation of steel during the thermal cycle. Ma and co-workers [31] used a novel heating system with multi-layer thermal insulation to prevent the effect of thermal electrons which allowed to capture a high quality image at elevated temperature. In a recent study, Nutter et al [32] studied bainite sheaf growth using in-situ TEM.

To gain information on how bainitic microstructure forms, an in-situ SEM microscopy experiment for observing the morphology of growing bainite regions was conducted. The results obtained from the experiments were then used for parameterizing the morphological parameters of the previously developed cellular automata (CA) microstructure model. The detailed microstructure models allow the possibility of describing phase morphology during cooling. This provides the understanding needed for the capability to design and to control microstructure and mechanical properties of complex advanced steels.

2. Materials and methods

2.1. Materials

A medium-carbon, low-alloy steel microalloyed with Nb was used in this study. The composition was as follows: 0.4 C, 0.2 Si, 0.25 Mn, 0.90 Cr, 0.50 Mo, and 0.013 Nb (mass percent). The studied material was initially cast in a vacuum-induction melting (VIM) furnace before being cut into a slab-shaped block ($51 \times 200 \times 75$ mm). After being reheated at 1200 °C for 3 h, the blocks were then rolled on a pilot rolling mill to a final thickness of 10 mm. For a pilot rolling, a two-stage thermomechanically controlled process was carried out: a 4-pass rough rolling stage from 1200 to 1100 °C (above the recrystallization stop temperature) with a total reduction of 48 percent, and a 4-pass finish rolling stage below the recrystallization stop temperature with a finish rolling temperature of 800 °C, just above the finish temperature for austenite formation (A_3). The rolled strip was immediately water quenched to 420 °C, then transferred to a furnace with the same temperature (coiling simulation), where it was allowed to cool down slowly (about 0.01 °C/s) in order to achieve a lower bainite microstructure. The final thickness of rolled plate was about 10 mm. More details on the thermomechanical process can be found in [33].

2.2. High temperature in-situ SEM

Microscope: A Quanta 200 ESEM FEG scanning electron microscope provided by the FEI company was used for the in-situ microstructural observation during the applied thermal cycle.

Furnace: To apply the heating part, a high-temperature Furna-SEM1300 furnace (developed by ICSM and NewTEC Scientific company) was employed. The furnace was placed into the microscope, as shown in supplementary file 1. The furnace is fully metallic and contains a platinum ring as a heating element. The ring is welded to the sample holder made of a platinum alloy. The sample was directly placed onto the sample holder. The sample temperature was measured by a Pt-PtRh10 thermocouple located 1 mm below the sample. Dedicated measurements, performed using both an IR camera and a pyrometer showed that the sample temperature measurement is within a + -5 °C interval at T = 1000 °C. The heating rate that can be achieved with the furnace is ranging from 1 °C/min to 10 °C/s. The cooling rate can be controlled up to 2 °C/s within the 1000–200 °C temperature range. The sample can also be cooled naturally using a copper-made cooling system to achieve an average cooling rate of 5 °C/s in the temperature window of 1000–400 °C which allows to observe the austenite to bainite transformation. Furthermore, the metallic structure of the furnace ensures the pressure in the SEM chamber remains below 15×10^{-3} Pa during the whole thermal cycle. No variation to the higher values of the vacuum is measured during the thermal cycle, indicating that there is no undesired outgassing in the SEM chamber.

Sample and thermal cycle: A rectangular piece $(10 \times 20 \times 10$ mm$)$ was cut from the rolled plate and ground down to a thickness of 150 μm using an automatic polisher machine. Subsequently, disks of 5 mm diameter and 150 μm thickness were punched from the plate and polished to a mirror-grade finish using a 0.1 μm colloidal silica solution. These polished plates were then sectioned into 1 to 2 mm^2 pieces for the in-situ SEM experiments. The sample was heated up to 1000 °C with a 5 °C/s heating and cooled naturally down to 500 °C (approx. 5 °C/s), maintained at this temperature for 10 min, then cooled down naturally to room temperature.

Back Scattered Electron collection, image capture and image processing: The collection of the back-scattered electrons (BSE) at high temperatures is ensured by the Karmen detector provided by the Crytur company [4]. BSE images were recorded on a unique zone of the sample. The best compromise between the image contrast and the noise-to-signal ratio was achieved while operating with a 20 kV acceleration voltage. The image series were aligned using the SIFT Fiji plugin [34]. The Noise2Void (N2V) Fiji plugin was used to denoise the raw images. The N2V method is a powerful, context aware, and flexible algorithm for image denoising. It uses artificial neural networks to learn about the properties of the images and how to best denoise them [35].

2.3. Ex-situ thermal cycle and microstructure characterization

Gleeble dilatometer: To separately provide the critical phase transformation temperatures and dilatometric data, a Gleeble 3800 thermomechanical simulator has been employed in order to simulate the exact same thermal cycle performed during in-situ SEM. For this purpose, a cylindrical sample with a diameter of 6 mm and length of 30 mm was used.

Ex-situ SEM – EBSD: In order to characterize the grain structure of the final microstructure, electron backscatter diffraction (EBSD) investigations were performed on the in-situ tested samples (without any further sample polishing) using a Sigma Zeiss field-emission scanning electron microscope (FESEM). EBSD mappings were captured using an accelerating voltage of 15 kV, a working distance of 15 mm, a tilt angle of 70° and a step size of 0.2 μm.

3. Theory

3.1. Bainite growth

The aim of the on-going modelling work is to build a simplified model for rapid calculations, which still incorporates the essential features of the bainite growth theory as cellular automata rules. The model describes the growth of bainite regions, as observed in the in-situ experiments. The regions comprise similarly oriented sheaves, which in turn are formed by nucleation and growth of subunits.

The growth of a bainite sheaf is initiated on the prior austenite grain boundaries by nucleation of a subunits. A bainite subunit grows to a certain size, arrested by the plastic deformation of the austenite. New subunits are nucleated at the tip of the previous subunits. The carbon is rapidly partitioned from the bainite to the regions located next to and between the subunits. The growth of a sheaf consists of the successive nucleation and growth of subunits, where the subunit nucleation is the rate-limiting step. The aspect ratio of a growing sheaf is constant. However, a sheaf can continue to thicken even if the longitudinal growth is stopped. [36].

Some commonly applied simplifying assumptions are made in the models. A constant ratio between the growth and nucleation rates was assumed in the same way as in [37]. In the mean field model, it was assumed that the transformation rate depends on temperature and previously transformed fraction but does not depend on the previous history of temperature changes [14,37]. In the current study, these assumptions serve as simplifications for building computationally fast models that still incorporate many of the essential features of bainite formation. The detailed (but computationally heavy) physically based model for bainite formation is under development [38], and it can be used in the future for building more accurate cellular automata rules for fast computations.

3.2. Mean field model

The mean field (MF) model described in references [14,17,19,39] was applied to simulate the overall austenite to bainite transformation during cooling, and it was applied in designing the cooling path used in the experiments. The MF model describes the instantaneous overall transformation rate as a function of the temperature and the previously transformed phase fraction.

In the MF model, the transformation start (assumed as 1% of bainite formed) was calculated by applying the Scheil's additivity rule [14,40], i.e. the transformation is estimated to start when $\sum_i \Delta t_i / \tau(T) = 1$, where Δt_i is the simulation time-step and $\tau(T)$ is the fitted function, described by Eq. (1).

$$\tau(T) = K(B_s - T)^m \exp\left(\frac{Q}{R(T + 273.15)}\right) \tag{1}$$

Where K, m and Q (activation energy) are fitting parameters, R is gas constant, and B_s is the bainite start temperature. After the transformation has started, the subsequent transformation kinetics was calculated by applying Eq. (2), as in [19]

$$\frac{d\chi}{dt} = (\chi_{max} - \chi)\left[\ln\left(\frac{\chi_{max}}{\chi_{max} - \chi}\right)\right]^{\frac{n-1}{n}} n k_{MF}(T)^{\frac{1}{n}} \tag{2}$$

Where χ is the transformed bainite fraction, n is the Avrami exponent, χ_{max} is the maximum bainite fraction and $k_{MF}(T)$ is the temperature dependent rate parameter, which is described in Eq. (3).

$$k_{MF}(T) = \exp(-a(T - b)^2 - c) \tag{3}$$

Where a, b and c are fitting parameters. As described in [19] the mean field transformation model was fitted to the experimental thermo-mechanical test results. The parameters shown in Table 1 were obtained.

3.3. Cellular automata model

In order to simulate the nucleation and growth, as well as the shapes of the growing bainitic regions, the previously developed cellular automata (CA) model was applied [1]. The kinetic parameters obtained from the MF model were partly used in defining the CA model parameters. As described in [1], the overall transformation rate obtained from the fitted MF model was divided into nucleation and growth rates in the CA model based on the experimental in-situ microscopy observations of the growing bainitic regions. Also, the observed morphology of the growing regions (fraction of the longitudinal growth speed of bainitic sheaf to the transverse growth speed) was used to parameterize the CA model. The nucleation and growth direction of a new sheaf are partly randomized, so multiple repetitions are calculated for each parameter combination to achieve statistically more reliable results. The model is presented concisely here and details are described in [1].

In the CA equations, rate parameter k_{CA} is split into nucleation and growth, in Eqs. (4) and (5).

$$k_{CA}(T) = k_{nucl}k_{growth} = \frac{N(T)}{V}G(T) \tag{4}$$

$$\frac{k_{nucl}}{k_{growth}} = R_b \tag{5}$$

where k_{nucl}, k_{growth} are the nucleation and growth part of the rate parameter, N is the nucleation rate, V is the volume of simulated

Table 1
Mean field model parameters [19].

| K	Bs (°C)	m	Q (kJ)	a	b	c	n
0.04915	657.6	0.8681	56.7	$1.2317 \cdot 10^{-4}$	469.2	3.374	1

region (thin slice), G is the growth rate and R_b is a fitting parameter describing the relation between nucleation and growth. The parameter can be used to emphasize either sheaf nucleation (many small sheaves) or sheaf growth rate (few large sheaves). This way the resulting morphology can be fitted to experimentally obtained microstructures.

The shape of a single sheaf is assumed to be a triangle. This growth geometry simplification allows to handily define the growth directions and speed mathematically. Sheaf growth speed is calculated as in Eq. (6)

$$v = \sqrt{\frac{G(T) \cdot 3L_{su}}{dz}} \tag{6}$$

where L_{su} is sheaf growth ratio (height/width) and dz is the volume of the simulation region. L_{su} is another parameter used to affect the microstructure morphology. Increasing the value of the parameter causes long, thin sheaves and decreasing it causes short, thick sheaves. Sheaf growth ratio also affects phase transformation kinetics through the impingement effect, because longer sheaves collide faster with high-angle grain boundaries, thus slowing the phase transformation rate [22].

A new equation, which describes the correspondence between the macroscopic MF and the 2-dimensional CA models is developed in the current article. The kinetics and morphology of the growing bainitic regions obtained with the CA model are shown to be in good agreement with the experimental observations. The fitted MF model describes the bainite formations in 3-dimensional material, where the Avrami exponent n is a fitting parameter. The CA model describes the bainite formation in a 2-dimensional slice of the material, assuming a triangular shape for the bainite region. For this reason, the Avrami exponent in the CA model is $n = 3$ (see [1] for details). In reality, in some cases, the maximum bainite fraction that can form may be limited because of the chemical and strain stabilization of the austenite, which is called the incomplete transformation phenomena, characterized by the maximum phase fraction that can be transformed χ_{max} [18]. In the CA model, there is no limitation for the maximum phase fraction. For this reason, $\chi_{max} = 1$ in the CA model. The kinetics described by the CA model must be equal to the kinetics of the MF model (Eq. (2)),
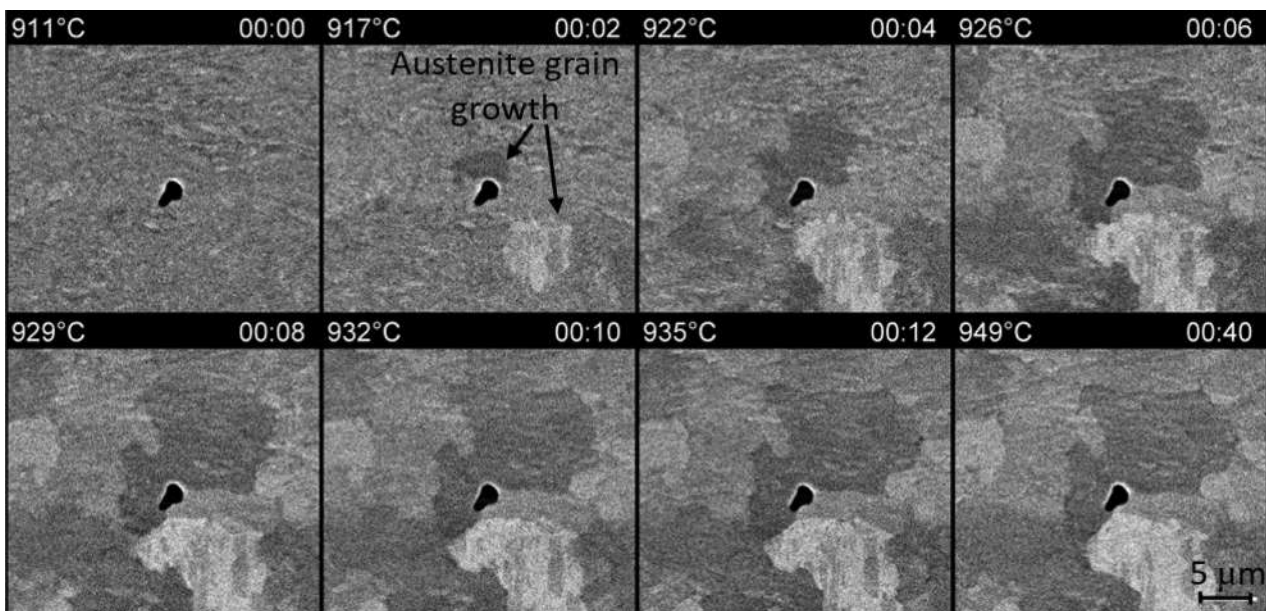
Fig. 1. Formation of austenite grains on the sample surface during heating.

$$(\chi_{max} - \chi)\left[\ln\left(\tfrac{\chi_{max}}{\chi_{max}-\chi}\right)\right]^{\frac{n-1}{n}} nk_{MF}(T)^{\frac{1}{n}} = (1-\chi)\left[\ln\left(\tfrac{1}{1-\chi}\right)\right]^{\frac{3-1}{3}} 3k_{CA}(T)^{\frac{1}{3}},$$

hence the rate parameter k_{CA} for the CA model can be calculated from Eq. (7)

$$k_{CA}(T) = \left[\frac{(\chi_{max}-\chi)\left[\ln\left(\tfrac{\chi_{max}}{\chi_{max}-\chi}\right)\right]^{\frac{n-1}{n}} nk_{MF}(T)^{\frac{1}{n}}}{(1-\chi)\left[\ln\left(\tfrac{1}{1-\chi}\right)\right]^{\frac{2}{3}} \cdot 3}\right]^3 \qquad (7)$$
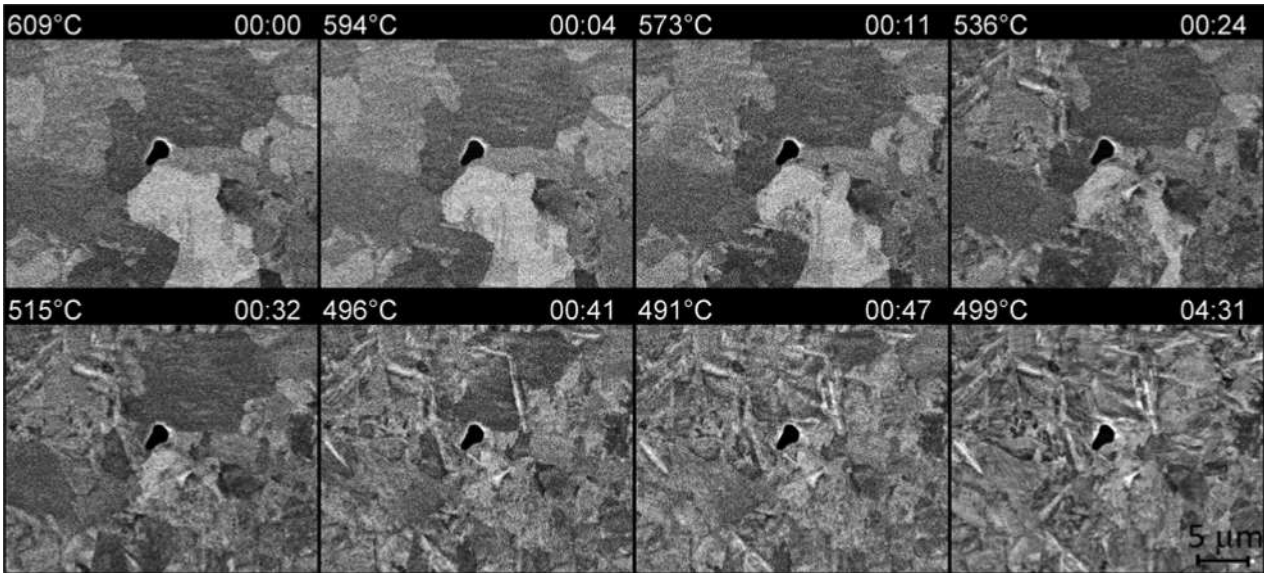
Fig. 2. Formation of bainite sheaves on the sample surface during cooling.
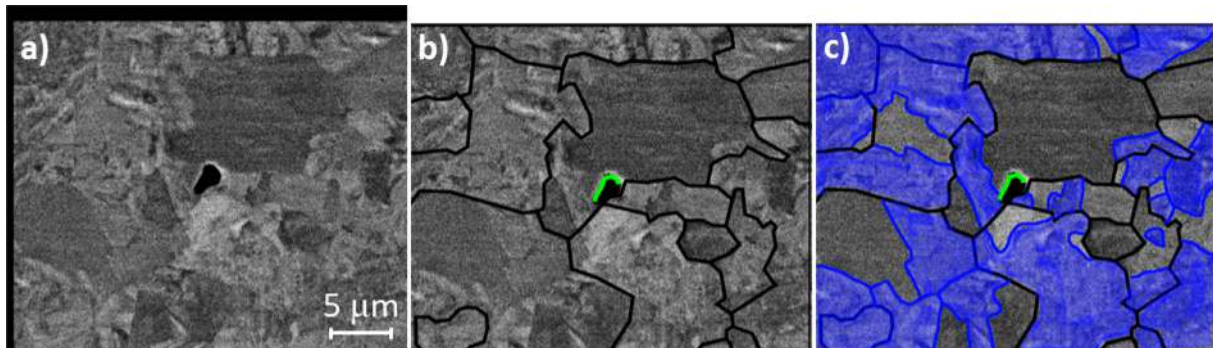
Fig. 3. In-situ image manual processing: a) raw image, b) prior austenite grain boundaries emphasized with black lines and c) bainite areas highlighted in blue. (For interpretation of the references to colour in this figure legend, the reader is referred to the web version of this article.)
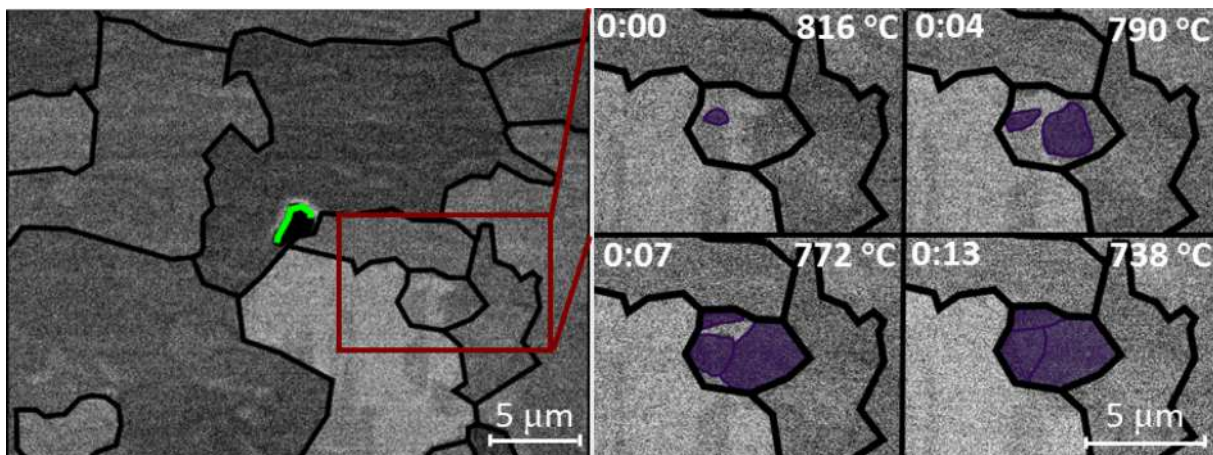

Fig. 4. Observed growth of polygonal ferrite.

where $k_{MF}(T)$ is the mean field model rate parameter [19]. For the current study and fitted model $\chi_{max} = 1$. Eq. (7) provides the correspondence between the MF model rate parameter and the 2–dimensional CA model rate parameter.

4. Results and discussion

4.1. In-situ SEM

Five experiments were performed on the as-received material using the same thermal cycle in order to check the reproducibility of the phenomena as well as to determine the best imaging conditions to observe the phase transformations. The image stacks are aligned and reported as movies (see supplementary file 2). First of all, one must note that no surface oxidation of the samples has been evidenced, indicating that the oxygen partial pressure in the SEM chamber always remains sufficiently low to overcome this difficulty.

The use of the BSE collection at high temperature allows observing phase transformations. The first transformation observed is the formation of austenite during the sample heating, shown in Fig. 1. The images show the formation of austenite grains, which is observed starting at 917 °C and is completed when the temperature reaches 949 °C. These observations are not in line with previous studies on the same material [19,41], so a dilatometer test was performed to evaluate the precise phase transformation temperature under the same thermal cycle.
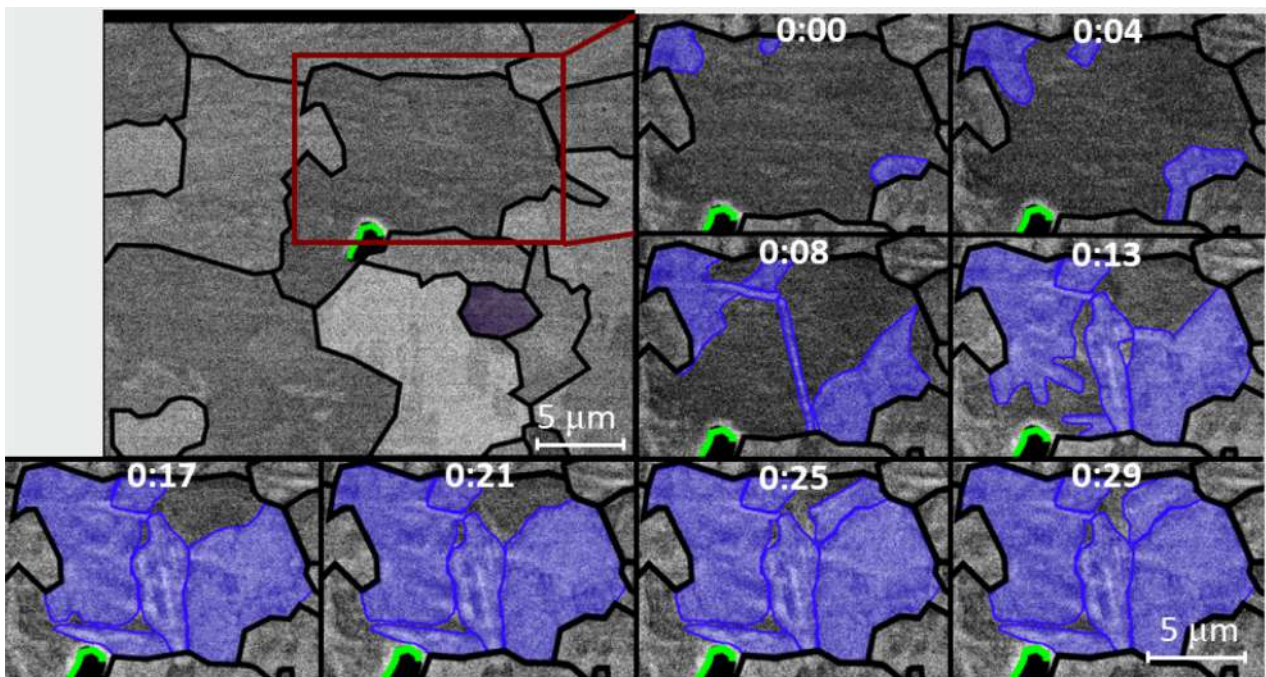

Fig. 5. Observed bainite growth of several sheaves, temperature $\sim$ 500 °C.
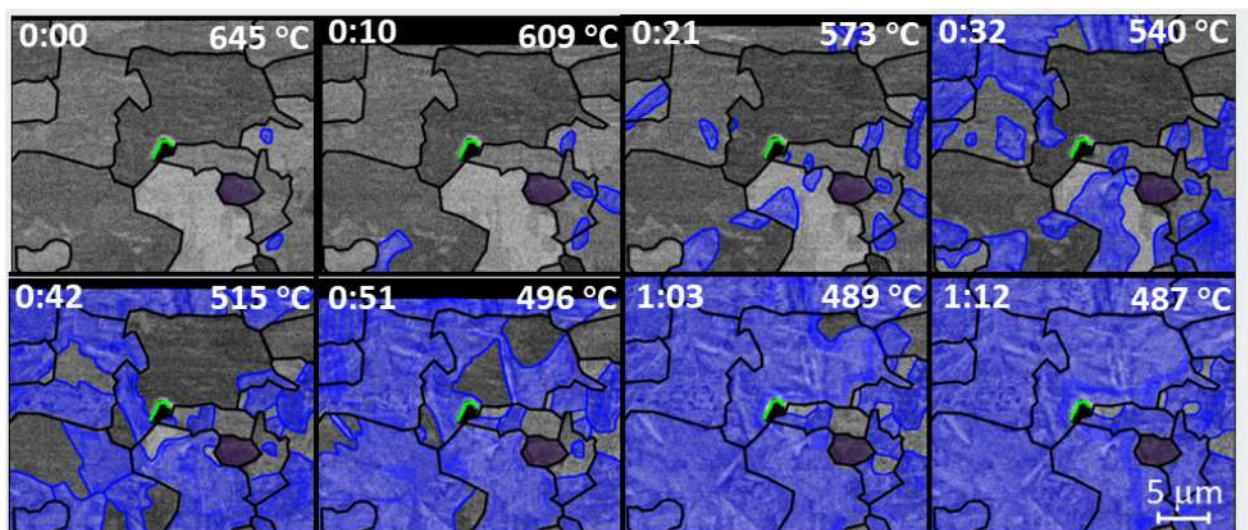

Fig. 6. Bainite sheaf transformation with bainite areas highlighted in blue and ferrite in purple. (For interpretation of the references to colour in this figure legend, the reader is referred to the web version of this article.)

When the sample is fully transformed into austenite, it is cooled naturally down to 500 °C and the formation of bainite sheaves from austenite grains is observed in Fig. 2. This phase transformation begins at 760 °C and is completed when temperature reaches 500 °C. Unlike austenisation, the bainitic phase transformation is in line with previous studies.

The image segmentation allows to discriminate between the zones corresponding to austenite and bainite. Phase fraction is calculated as the surface ratio of transforming phase relative to the area of the whole image. The variation of the surface coverage of austenite and bainite during their formation are calculated to estimate phase transformation kinetics as a function of time. In Fig. 3, the manual processing of images is presented. First, the austenite grain boundary lines are drawn to a fully austenitic image (taken right before the start of bainite transformation) as a separate layer, which is copied to the partially bainitic image and aligned with the black smudge in the middle of the image using the green line. Next, the image topography is compared to a fully austenitic state and

any topography changes are interpreted as phase transformation. The transformed areas are highlighted in blue.

A minor amount of polygonal ferrite growth was observed in the in-situ images during cooling from 816 to 738 °C, shown in Fig. 4. The temperature is in accordance with the mean field simulation of the result. Note that the three ferrite grains appear within a single austenite grain.

A small area of the images was chosen for closer inspection. Fig. 5 shows the area marked with a red rectangle and a slide show of the growth stages. These bainite sheaves can be used to compare the in-situ experiment results to other methods in this paper.

In Fig. 6, the whole image bainite areas are marked without separating growing sheaves from each other. The combined surface coverage of the highlighted areas is interpreted as the fraction of bainite transformation. With the images in Fig. 6, the fraction of bainite as a function of time is obtained.

For comparison, CA model results for the best fitted parameter combination are shown in Fig. 7. The images are chosen so that
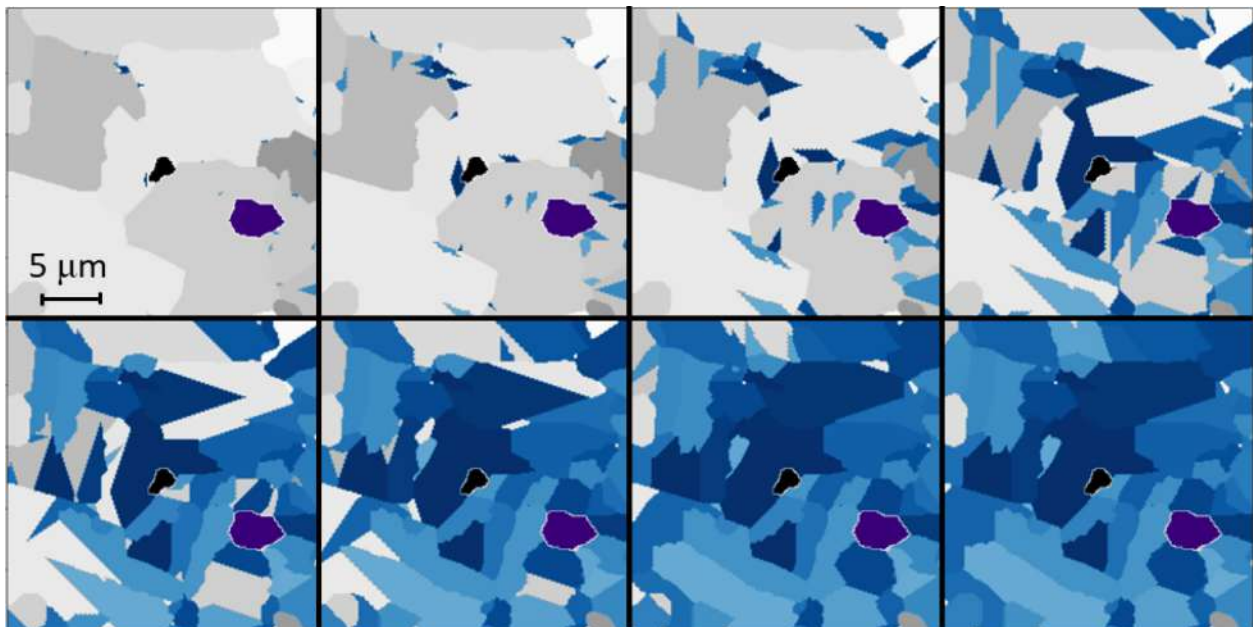

Fig. 7. Bainite sheaf transformation as calculated with CA model, case Lsu2 | Rb40.
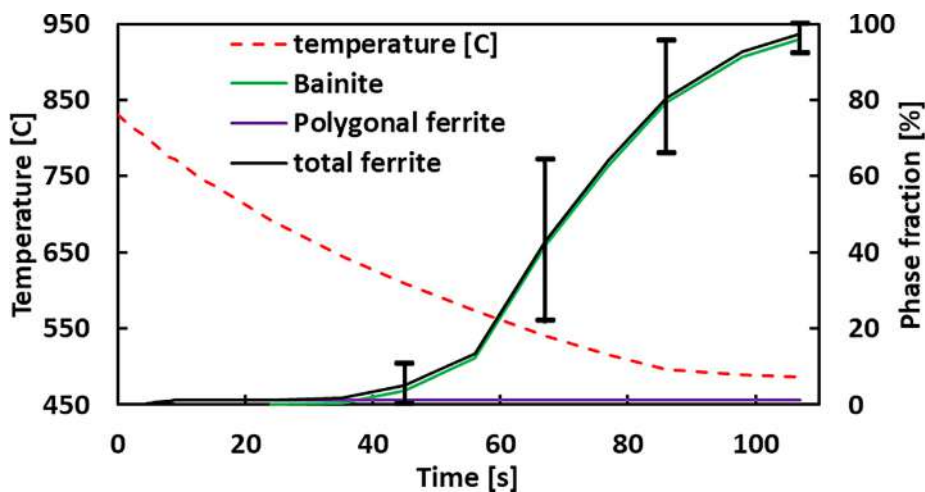

Fig. 8. In-situ temperature paths and estimated bainite fraction during cooling.

they correspond with transformed phase fractions in Fig. 6 and the images are scaled to the same size. See supplementary file 3 for full video.

The temperature path of the in-situ test and estimated phase fractions of bainite are shown in Fig. 8 for the cooling stage. During heating, the microstructure transforms to fully austenitic and during cooling the microstructure transforms mostly to bainite with a minor amount (~2 %) of visible polygonal ferrite. Since it was possible to observe only one location in the in-situ experiment, the amount of error for the phase transformation kinetics was estimated by dividing the observed area to four quadrants. For each quadrant the fraction of phase formed was calculated. Standard deviation was calculated with all quadrants, they are shown with the error bars in Fig. 8.

4.2. Dilatometry data

The in-situ test produces interesting results, but they need to be compared with well-founded experimental methods. In this study, the dilatometer test was chosen to study phase transformation kinetics of the bulk materials. The thermal cycle for the dilatometer test was chosen to imitate the in-situ test heating and cooling rates as well as holding temperatures with reasonable accuracy. Fig. 9 shows the comparison of the thermal cycles of both tests.

Dilatometer test measures the thermal expansion and contraction of the test sample during the thermal cycle. With a steady heating or cooling rate the change is linear, so non-linear behaviour can be assumed to result from phase transformation. In Fig. 10, the dilatometer test results are presented. Fig. 10a) shows
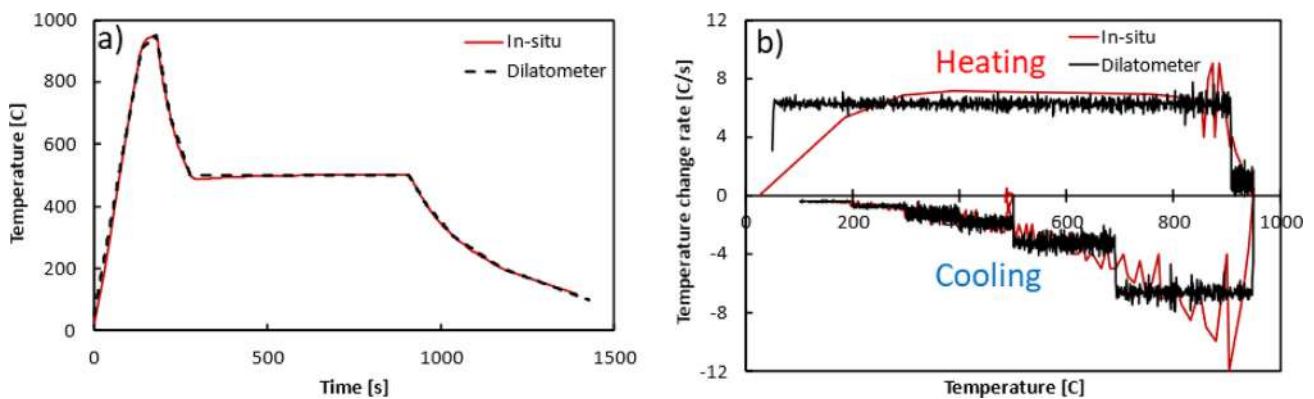

Fig. 9. Heating and cooling cycles of in-situ tests and Gleeble dilatometry tests.
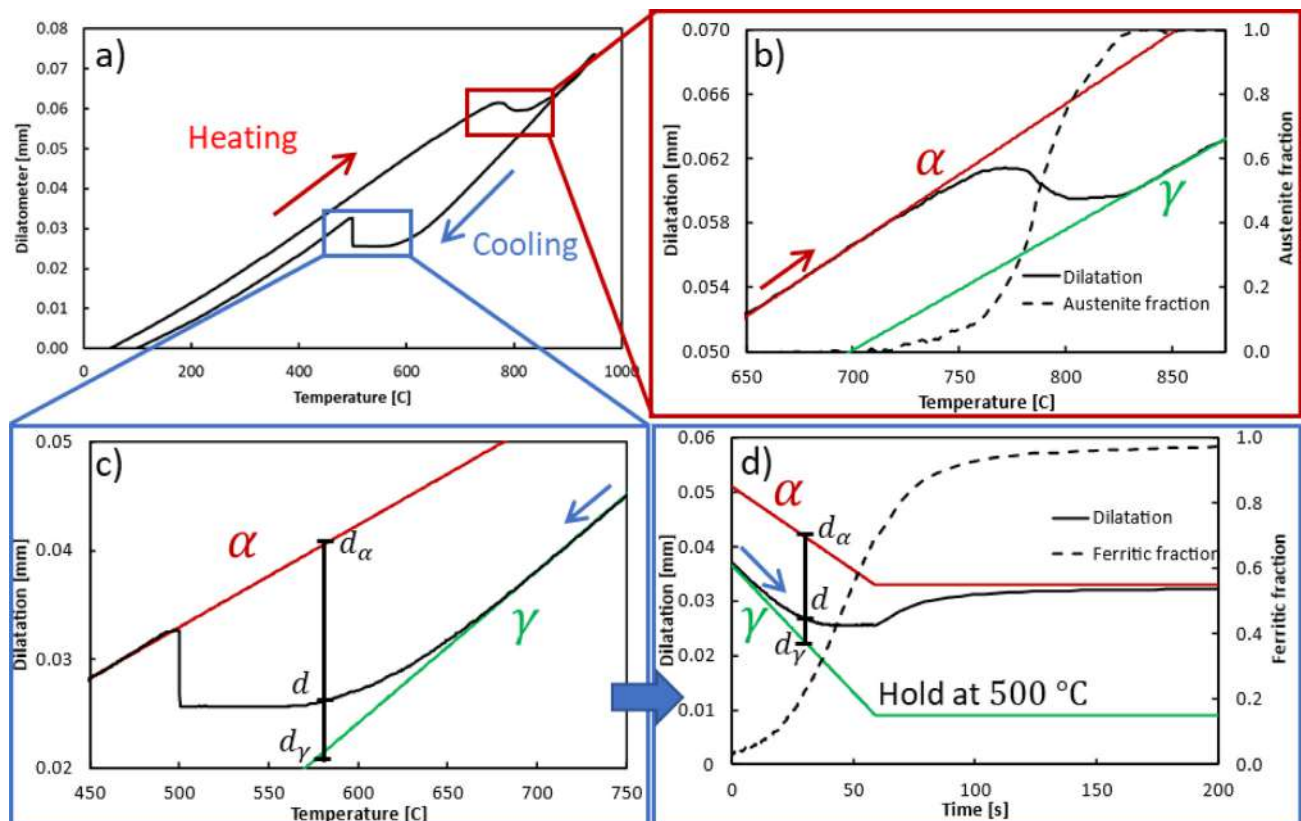

Fig. 10. A) dilatometer full test, b) austenite transformation, c) ferritic transformation with temperature, d) ferritic transformation with time.

the overall dilatometer curve during both heating and cooling. Fig. 10b) shows the dilatometer curve in a non-linear section during heating and helper lines have been fitted to linear areas before and after the non-linear section, depicting ferrite (red line) and austenite (green line) thermal expansion. Using the lever rule, phase transformation can be calculated, and the resulting austenite fraction is depicted by the dashed black line. Fig. 10c) shows the dilatometer curve in a non-linear section during cooling in the same way as Fig. 10b). The thermal cycle includes a holding period at 500 °C during cooling, so the lever rule is applied to Fig. 10d) where the same area is shown as a function of time and phase transformation can be calculated.

4.3. Ex-situ EBSD

The in-situ SEM final bainitic microstructure is compared to ex-situ EBSD data, obtained from the same sample at room temperature. Fig. 11 presents the EBSD results including image quality (IQ) map (Fig. 11a) and inverse pole figures (IPF) map (Fig. 11b). The grain structure with a misorientation angle higher than 15° were constructed and overlayered on both maps (high angle grain boundaries plotted in solid black lines).

As observed in the EBSD results, there are some very small bainite subunits which considered as a grain as well as other oddly shaped grains, like the highlighted grain in Fig. 11c). It seems like
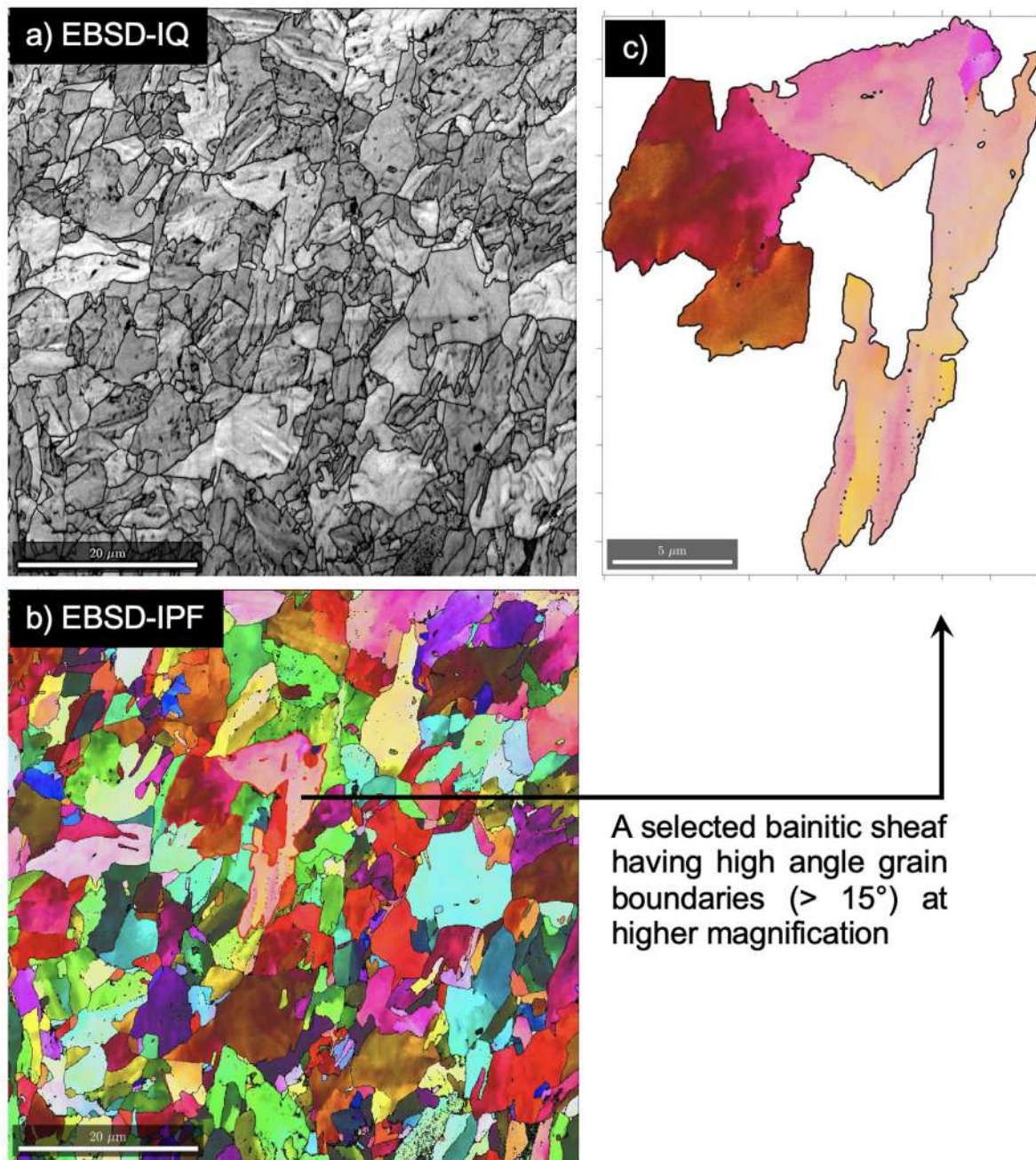

Fig. 11. EBSD image as analyzed by the TSL OIM -software.

two separate grains have been joined together, probably because of similar grain orientation. These results may not generate trustworthy results regarding the bainitic grain size distribution and directly comparing grain surface areas to the CA model results would produce unreliable results since in the CA model the distinct sheaves are always calculated as separate regions, so other methods for comparing grain sizes were investigated. After some initial comparison to modeling results, linear intercept interval distribution was found to be a good way to compare the data. This comparing method is based on the mean linear intercept (MLI) method, presented in [42]. Traditionally the MLI method is done manually, but in this case, the data is digital with well-defined grain boundaries, so the process can be completely automated.

First, the EBSD data is converted from point data to a cell structure, similar to CA. This allows using the same calculation script for both the EBSD data and the CA data. Then measure lines are drawn horizontally and vertically at regular intervals. The cells on a measure line are checked in sequence, and when the grain ID on a cell changes from the previous cell, a grain boundary has been found

and a linear intercept is marked. This way each measure line is analyzed. Fig. 12a) includes the result of the MLI analysis procedure. A dataset is formed of linear intercept intervals, which is the distance between consecutive intercepts. The dataset distribution is presented in this study as a histogram, shown in Fig. 12b).

4.4. Modeling – Kinetics

Phase transformation kinetics were modelled using both the mean field and CA methods. The mean field model is fitted to the experimental data, and the CA method uses parameters that are partly calculated from the mean field model and partly from the geometry and number of observed bainite regions to control the phase transformation rate.

The mean field model parameters are obtained in previous studies of the same material [19]. Fig. 13 includes ferrite and bainite growth as predicted by the mean field model and the experimental result (black line) based on the dilatometry test. There is some discrepancy between the observed and modelled transfor-
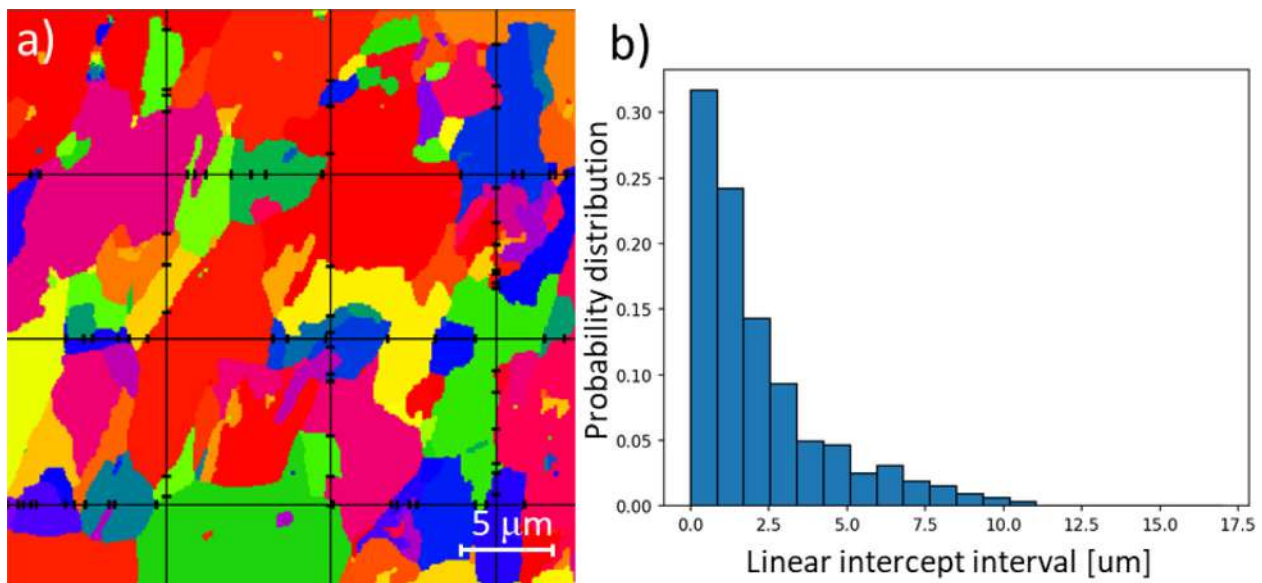

Fig. 12. A) ebsd image (zoomed-in) with linear intercept markings and b) linear intercept interval distribution of ebsd image.
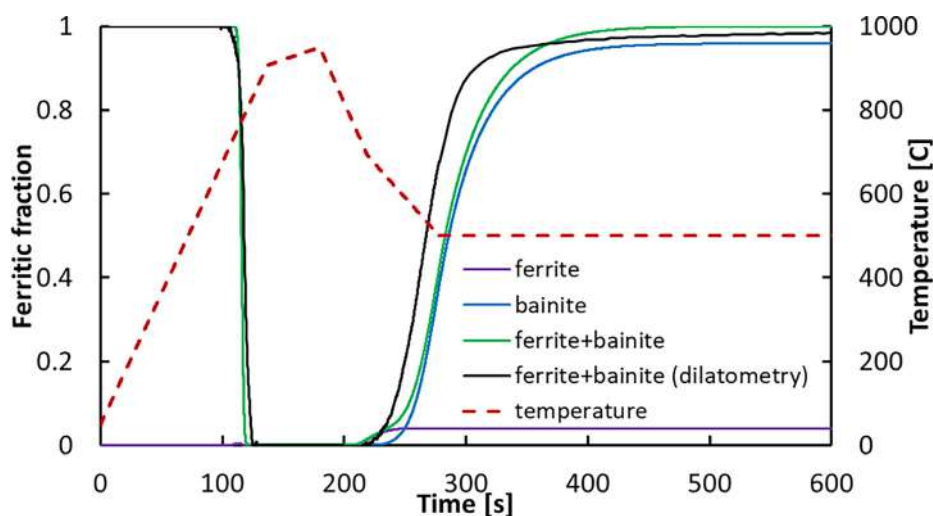

Fig. 13. Dilatometry data and mean field simulation.

mation kinetics. The observed kinetics curve for bainite formation starts somewhat later (at slightly lower temperature) in the mean field model than in reality. Most likely, the parameters that were fitted for the continuous cooling tests in [19] yielded a function, which was inaccurate in the temperature range 625–650 °C, where bainite seems to form earlier in reality. However, once the temperature is below 625 °C, the transformation rate seems to agree with the experimental data.

For the CA method, a simulation test series was created with values for L_{su} 2, 6, 10 and R_b 5.0–800.0 and 60 repeats of each test case to improve the statistical validity of the data. The starting point for each simulation is the austenitic microstructure obtained from the in-situ test and the same thermal cycle is used. Phase transformation kinetics can be calculated for each time step by dividing the ferritic fraction area with the total simulation area. Kinetics obtained this way for all repeats of L_{su} 2, R_b 40.0 are pre-
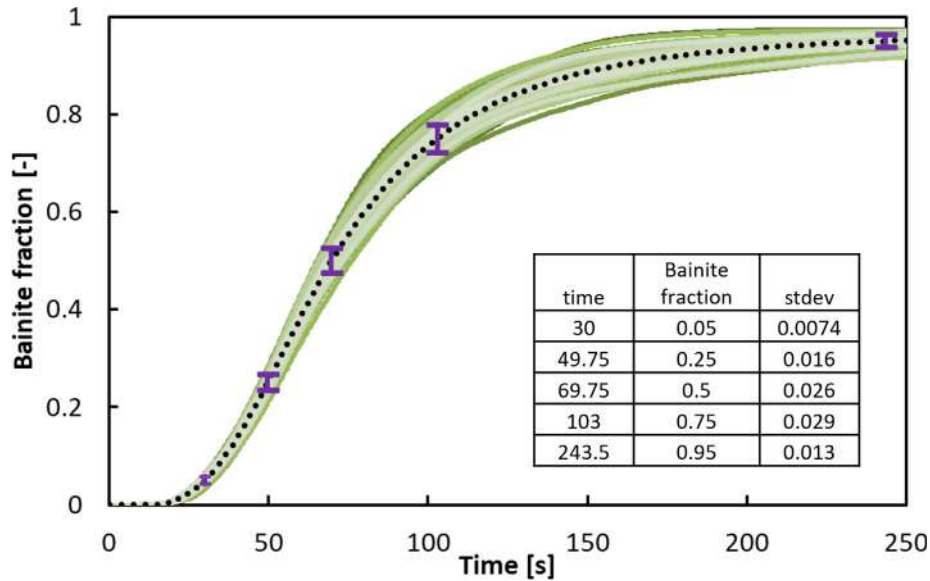

Fig. 14. CA example case (L_{su} 2, R_b 40.0) with 60 repeats (green lines), their average (black dashed line) and standard deviation as error bars in selected phase fractions. (For interpretation of the references to colour in this figure legend, the reader is referred to the web version of this article.)
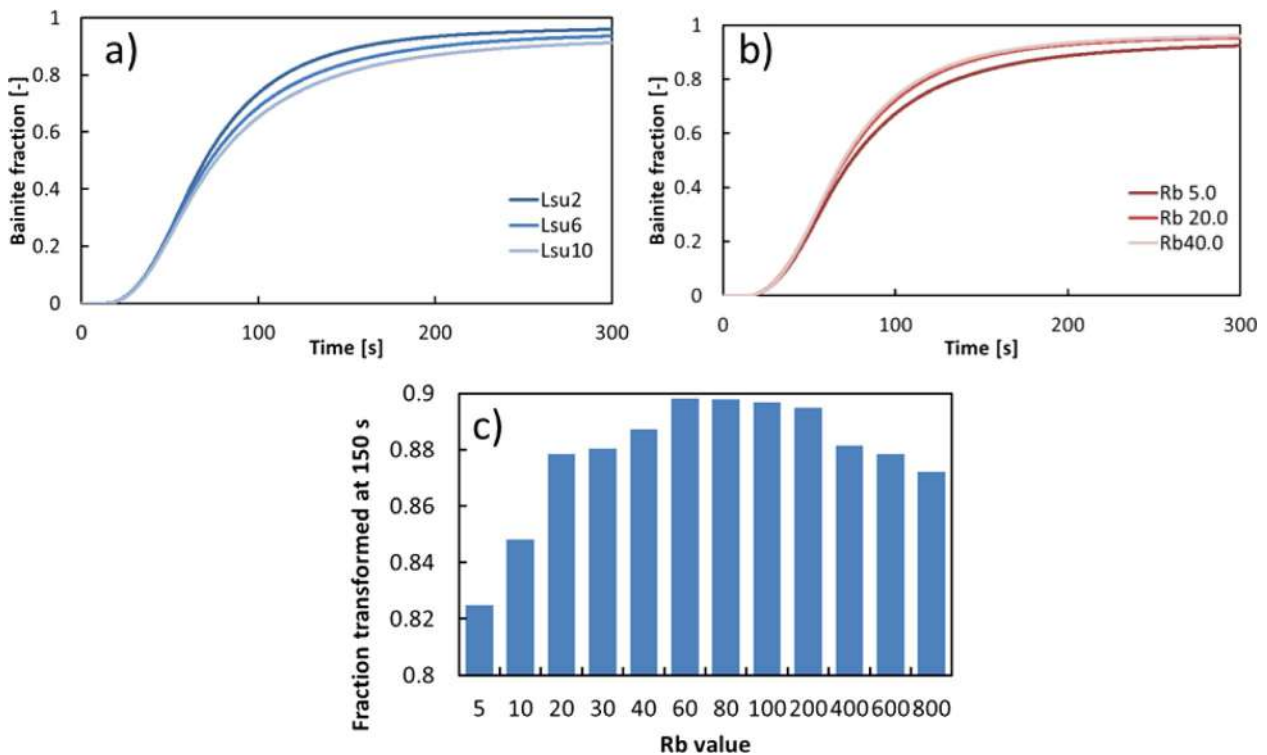

Fig. 15. Averaged values of the CA results with model parameters a) R_b = 40.0 and b) L_{su} = 2. c) Fraction transformed at 150 s with various R_b values.

sented in Fig. 14 to exemplify the randomness associated with the numerical model. The black dashed line in the figure is the average of all the repeats, and standard deviation is calculated for selected phase fractions, indicated by the error bars and values in the table of Fig. 14.

Effect of simulation parameters on kinetics is discussed in more detail in [22]. Similar observations have been made in the current study, and Fig. 15 shows the effect of test parameters, a) shows the effect of L_{su}, with b) and c) showing the effect of R_b. R_b seems to show no significant effect on phase transformation kinetics between values 20 and 400, with smaller values slowing down nucleation and higher values slowing sheaf growth disproportionally. Increasing L_{su} has a retarding effect on the phase transformation rate. This is caused by impingement of the sheaves and the effect increases as the length-wise growth increases.

The experimental in-situ and dilatometer phase transformation kinetics are compared with the simulated mean field and CA model kinetics in Fig. 16. It appears that there is some amount of inaccuracy in the mean field model (which had been fitted to the CCT experiments in the previous study [10]) above temperature 625 °C. To compare the simulated kinetics curve with the curve obtained from the dilatometry measurements at temperature range below 625 °C, the offset caused by the transformation occurring at higher temperature is removed in Fig. 16 b) and d), as indicated by the arrows in a). This comparison of the kinetic curves shows the good agreement between the transformation rate below 625 °C. The CA model results are averaged as shown in Fig. 14 and compared to mean field data, and case Lsu2 | Rb40 was found to be close to the MF kinetics. When comparing the in-situ results to other data, it must be kept in mind that the studied area is a freely expanding two-dimensional surface, which inevitably behaves differently than the bulk material which is constrained from all direc-

tions. That being said, the dilatometry and in-situ curves are quite nicely in line with each other.

4.5. Modeling – Microstructure

The CA model was used to calculate microstructural evolution during phase transformation. The rate parameter, which affects the kinetics through equations (4) and (5) were obtained from the mean field model. Linear intercept interval distributions were calculated for each test case in the way described in the EBSD results section. The distributions between CA and EBSD were compared for each test case, and the results are shown in Fig. 17. The first bin was filtered out of the comparison as the results of that size are mostly artefacts. The bin sizes were fixed, so numerical comparison was done by simply adding up the bin differences for each test case $BD = \Sigma_i \left| B_i^{EBSD} - B_i^{CA} \right|$, where B_i^{EBSD} and B_i^{CA} are bin values for the EBSD and CA data respectively. L_{su} 2 was deemed the best case when considering transformation kinetics, and when comparing the different R_b cases, it was found that R_b 40 shows minimum bin difference to the EBSD results. The best case with the chosen criteria is then L_{su} 2 | R_b 40, which is marked with a green dashed ellipse.

A visual comparison of the final microstructure with in-situ, CA and EBSD is shown in Fig. 18. The images are shown in the same length scale, and it can be seen that the general sheaf size is quite close in all cases. In-situ and CA images have the prior austenite grain boundary included for clarity. The different colors in CA represent bainite instances and have no further meaning, whereas the EBSD image colors mean the instance orientation. The small austenite regions around the CA simulation area are caused by
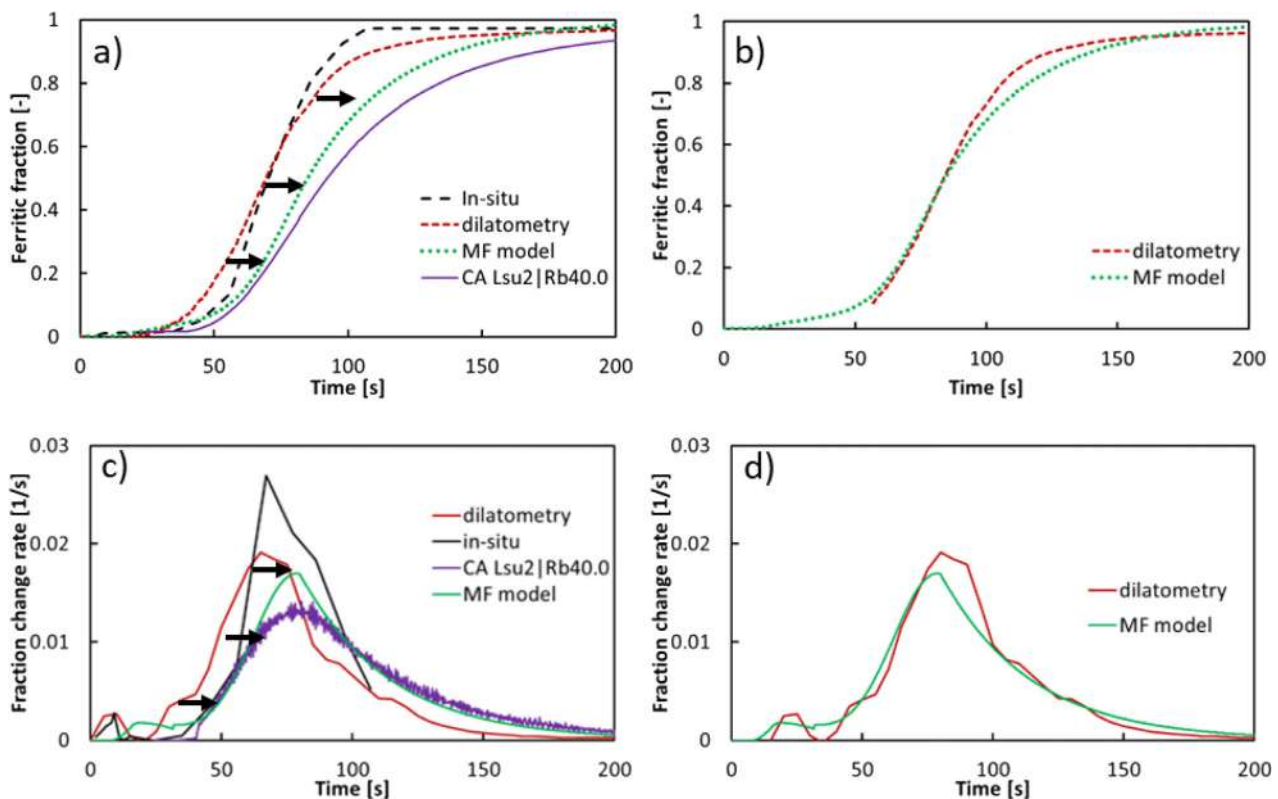
Fig. 16. A) comparison of phase transformation kinetics. the arrows indicate offset caused by the mean field model inaccuracy at higher temperature range 625–650 °C (see text for details). b) The kinetics comparison at temperatures below 625 °C, where the offset has been removed. c) the transformation rate corresponding to a). d) the transformation rate corresponding to b).
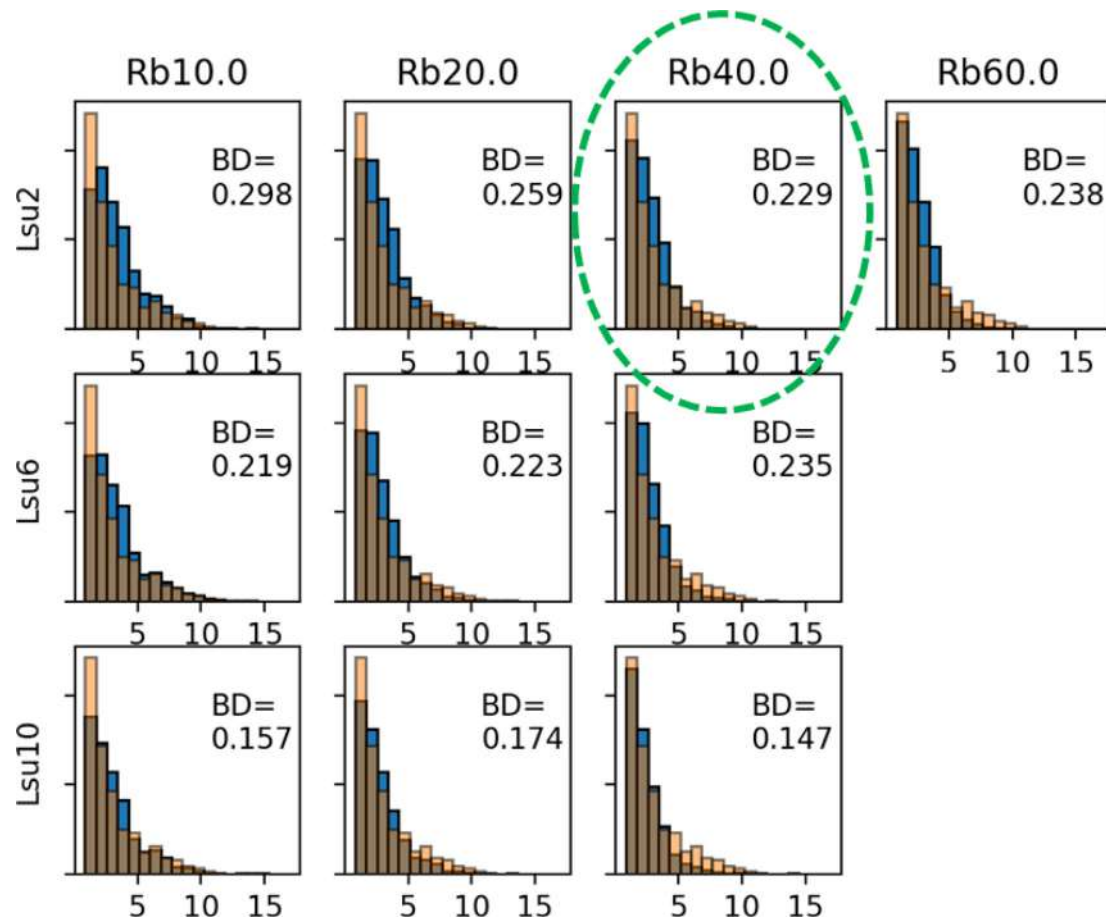
Fig. 17. Bainite sheaf size distribution, EBSD (orange) vs. CA (blue). The green dashed ellipse is the best case based on a combination of kinetics comparison and bin difference. (For interpretation of the references to colour in this figure legend, the reader is referred to the web version of this article.)
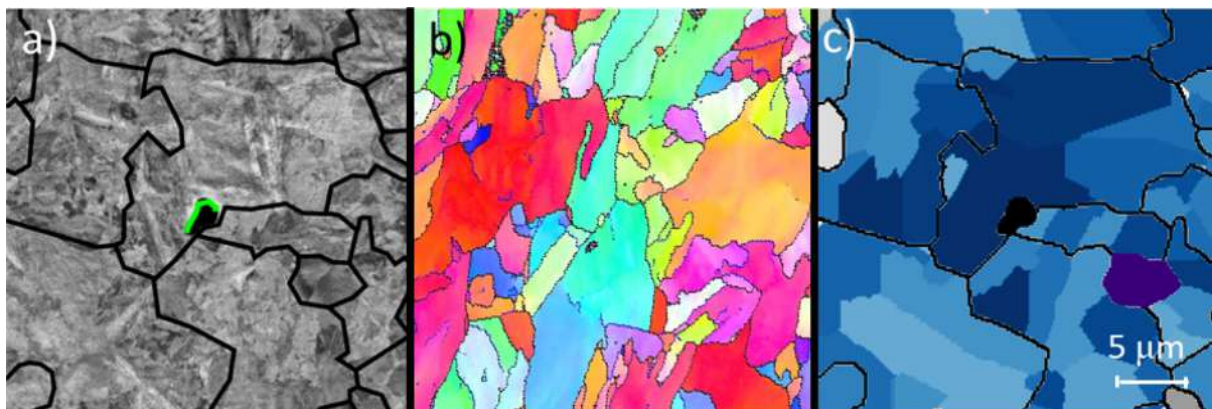
Fig. 18. Microstructure images with scales matched for a) in-situ, b) EBSD and c) CA case Lsu2 | Rb40.

the fixed time limit of the simulation, which was added to prevent absurdly long computational times.

5 Conclusions and outlook

The in-situ method presented in this article provides direct observation of the initiation and growth of phase regions in the length scale of 10 µm. Transformation kinetics and the evolution of phase morphology can simultaneously be studied with the same

experiment. It is especially interesting to be able to observe the initiation and the impingement of the growing bainite regions, since these aspects have a decisive influence on the dynamics of the phase formation. The test is quite demanding and time-consuming and the data it produces is difficult to process and analyse due to the constantly changing focus of the microscope and the high amount of noise in images. Despite these limitations, the experimental in-situ method provides important information on the phase formation dynamics, which is not attainable with the usual ex-situ investigations. Using the combination of the in-situ

and ex-situ methods, a comprehensive understanding of the phase formation phenomena emerges.

The dilatometer test was used to compare phase transformation kinetics to the in-situ results. It was seen that during heating in the in-situ test, the changes in the grain morphology were observed at clearly higher temperature than in the dilatometer test. For this reason, the in-situ observation most likely corresponds to the grain growth stage. The information about the austenite grain structure is useful since it affects bainite formation greatly.

The bainitic transformation with a minor amount of ferrite was observed with the in-situ test. The phase transformation kinetics agreed quite nicely with the dilatometry results as well as the modelled results. The morphology of the bainite regions appears quite similar as the EBSD data and the parameterised CA results.

The mean field and CA models both produced phase transformation data quite similar to experimental methods, although some difference can be seen. CA model parameters were calibrated to find a good agreement to the EBSD and in-situ images. Linear intercept interval distributions of CA and EBSD were compared against each other to find the parameter combination that best describes the observed morphology. A satisfactory comparison method was found, and a good correspondence was found between the model and experimental data.

The in-situ method was compared to well-founded experimental ex-situ methods and previously developed models. Obtained results are promising and show that the in-situ provides new important insights to the phase transformation dynamics by allowing direct observation of bainite sheaf growth and impingement. These results can be used in parameterising the CA model and can certainly be used to gain new knowledge of phase transformation in future studies. With some improvements in the image processing, growth of phase instances can be studied in more detail. Studying the statistical error of the in-situ method is also an important part of future studies.

In addition to the nucleation, growth and impingement of bainite modelled by the current fast model, the partitioning and diffusion of carbon and the effect of transformation strains are important phenomena, which have been considered in a more detailed but computationally much more demanding model [38].

Current trend of steel development is leading towards very complex steels with multiple phases, which have microstructures that are very difficult to study just by using previous methods that can only study the final microstructure or the macro-scale phase transformation kinetics. The in-situ method could prove to be an invaluable addition to a metallurgist's toolbox by studying the dynamically interactive formation of each phase. This information can be used to improve current phase transformation models and the resulting phase morphologies could be linked to material mechanical properties in future studies.

Data availability

All data are available upon reasonable request by contacting the corresponding author.

Data availability

Data will be made available on request.

Declaration of Competing Interest

The authors declare that they have no known competing financial interests or personal relationships that could have appeared to influence the work reported in this paper.

Acknowledgements

Appendix A. Supplementary material

Supplementary data to this article can be found online at https://doi.org/10.1016/j.matdes.2023.111956.

References

[1] O. Seppälä, A. Pohjonen, A. Kaijalainen, J. Larkiola, D. Porter, Simulation of bainite and martensite formation using a novel cellular automata method, Procedia Manuf. 15 (2018) 1856–1863, https://doi.org/10.1016/j.promfg.2018.07.204.

[2] R. Podor, G.I.N. Bouala, J. Ravaux, J. Lautru, N. Clavier, Working with the ESEM at high temperature, Mater. Charact. 151 (2019) 15–26, https://doi.org/10.1016/j.matchar.2019.02.036.

[3] R. Podor, X. Le Goff, J. Lautru, H.-P. Brau, M. Barreau, X. Carrier, J. Mendonça, D. Nogues, A. Candeias, Direct Observation of the Surface Topography at High Temperature with SEM, Microsc. Microanal. 26 (3) (2020) 397–402.

[4] R. Podor, J. Mendonça, J. Lautru, H.P. Brau, D. Nogues, A. Candeias, P. Horodysky, A. Kolouch, M. Barreau, X. Carrier, N. Ramenatte, S. Mathieu, M. Vilasi, Evaluation and application of a new scintillator-based heat-resistant back-scattered electron detector during heat treatment in the scanning electron microscope, J. Microsc. 282 (2021) 45–59, https://doi.org/10.1111/jmi.12979.

[5] L. Rauch, R. Kuziak, M. Pietrzyk, From high accuracy to high efficiency in simulations of processing of dual-phase steels, Metall. Mater. Trans. B Process Metall. Mater. Process. Sci. 45 (2014) 497–506, https://doi.org/10.1007/s11663-013-9926-5.

[6] M. Umemoto, K. Horiuchi, I. Tamura, Pearlite Transformation during Continuous Cooling and Its Relation to Isothermal Transformation, Trans. Iron Steel Inst. Japan. 23 (1983) 690–695, https://doi.org/10.2355/isijinternational1966.23.690.

[7] B. Donnay, Microstructure evolution of C-Mn steels in the hot-deformation process: the stripcam model, in: 2 Nd Int. Conf. Model. Met. Roll. Process., 1996.

[8] M. Militzer, E.B. Hawbolt, T.R. Meadowcroft, Microstructural model for hot strip rolling of high-strength low-alloy steels, Metall. Mater. Trans. A Phys. Metall. Mater. Sci. 31 (2000) 1247–1259, https://doi.org/10.1007/s11661-000-0120-4.

[9] S. Serajzadeh, Prediction of temperature distribution and phase transformation on the run-out table in the process of hot strip rolling, Appl. Math. Model. 27 (2003) 861–875, https://doi.org/10.1016/S0307-904X(03)00085-4.

[10] M. Pietrzyk, J. Kusiak, R. Kuziak, Ł. Madej, D. Szeliga, R. Gołąb, Conventional and Multiscale Modeling of Microstructure Evolution During Laminar Cooling of DP Steel Strips, Metall. Mater. Trans. A Phys. Metall. Mater. Sci. 45 (2014) 5835–5851, https://doi.org/10.1007/s11661-014-2393-z.

[11] X. Chen, N. Xiao, D. Li, G. Li, G. Sun, The finite element analysis of austenite decomposition during continuous cooling in 22MnB5 steel, Model. Simul. Mater. Sci. Eng. 22 (6) (2014), https://doi.org/10.1088/0965-0393/22/6/065005.

[12] X. Chen, N. Xiao, M. Cai, D. Li, G. Li, G. Sun, B.F. Rolfe, A Modified Approach to Modeling of Diffusive Transformation Kinetics from Nonisothermal Data and Experimental Verification, Metall. Mater. Trans. A Phys. Metall. Mater. Sci. 47 (2016) 4732–4740, https://doi.org/10.1007/s11661-016-3608-2.

[13] H. Zhao, X. Hu, J. Cui, Z. Xing, Kinetic Model for the Phase Transformation of High-Strength Steel Under Arbitrary Cooling Conditions, Met. Mater. Int. 25 (2019) 381–395, https://doi.org/10.1007/s12540-018-0196-2.

[14] A. Pohjonen, M. Somani, D. Porter, Modelling of austenite transformation along arbitrary cooling paths, Comput. Mater. Sci. 150 (2018) 244–251, https://doi.org/10.1016/j.commatsci.2018.03.052.

[15] J. Ilmola, A. Pohjonen, S. Koskenniska, O. Seppälä, O. Leinonen, J. Jokisaari, J. Pyykkönen, J. Larkiola, Coupled heat transfer and phase transformations of dual-phase steel in coil cooling, Mater. Today Commun. 26 (2021) 101973.

[16] A. Pohjonen, A. Kaijalainen, J. Mourujärvi, J. Larkiola, Computer simulations of austenite decomposition of hot formed steels during cooling, Procedia Manuf. 15 (2018) 1864–1871, https://doi.org/10.1016/j.promfg.2018.07.203.

[17] A. Pohjonen, J. Paananen, J. Mourujärvi, T. Manninen, cooling Computer Simulations of Austenite Decomposition of Microalloyed 700 MPa Steel During Cooling, 090010 (2018). https://doi.org/10.1063/1.5034936.

[18] A. Pohjonen, P. Kaikkonen, O. Seppälä, J. Ilmola, V. Javaheri, T. Manninen, M. Somani, Numerical and experimental study on thermo-mechanical processing of medium-carbon steels at low temperatures for achieving ultrafine-structured bainite, Materialia. 18 (2021), https://doi.org/10.1016/j.mtla.2021.101150 101150.

[19] V. Javaheri, A. Pohjonen, J.I. Asperheim, D. Ivanov, D. Porter, Physically based modeling, characterization and design of an induction hardening process for a new slurry pipeline steel, Mater. Des. 182 (2019), https://doi.org/10.1016/j.matdes.2019.108047 108047.

[20] A. Pohjonen, V. Javaheri, J. Paananen, J. Pyykkönen, Semi-Automatic Optimization of Steel Heat Treatments for Achieving Desired Microstructure, Proc. 61st SIMS Conf. Simul. Model. SIMS 2020, Sept. 22-24, Virtual Conf. Finland, Linköping Electron. Conf. Proc. 176 19. (2021) 139–145.

[21] A. Pohjonen, Numerical simulations of gradient cooling technique for controlled production of differential microstructure in steel strip or plate, AIMS Mater. Sci. 8 (2021) 852–866, https://doi.org/10.3934/MATERSCI.2021052.

[22] O. Seppälä, A. Pohjonen, J. Larkiola, Effect of Anisotropic Growth and Grain Boundary Impingement on Bainite Transformation Models, Proc. 61st SIMS Conf. Simul. Model. SIMS 2020, Sept. 22-24, Virtual Conf. Finl. 176 (2021) 146–152. https://doi.org/10.3384/ecp20176146.

[23] J. Opara, R. Kuziak, Study of phase transformations in complex phase steel using a mesoscale cellular automaton model Part I: Modeling Fundamentals, J. Met. Mater. 72 (2020) 17–31, https://doi.org/10.32730/imz.2657-747.20.3.2.

[24] C. Bos, M.G. Mecozzi, J. Sietsma, A microstructure model for recrystallisation and phase transformation during the dual-phase steel annealing cycle, Comput. Mater. Sci. 48 (2010) 692–699, https://doi.org/10.1016/j.commatsci.2010.03.010.

[25] L. Madej, M. Sitko, K. Perzynski, L. Sieradzki, K. Radwanski, R. Kuziak, Multi scale cellular automata and finite element based model for cold deformation and annealing of a ferritic-pearlitic microstructure, Multiscale Mater Model, Approaches to Full Multiscaling 77 (2016) 235–254, https://doi.org/10.1515/9783110412451_014.

[26] S.M. Elahi, R. Tavakoli, I. Romero, D. Tourret, Grain growth competition during melt pool solidification—Comparing phase-field and cellular automaton models, Comput. Mater. Sci. 216 (2023) 111882.

[27] M.J. Peet, H.K.D.H. Bhadeshia, Surface relief due to bainite transformation at 473 K (200 °c), in: Metall. Mater. Trans. A Phys. Metall. Mater. Sci., Springer, 2011: pp. 3344–3348. https://doi.org/10.1007/s11661-011-0755-3.

[28] G. Mao, R. Cao, X. Guo, Y. Jiang, J. Chen, In situ observation of kinetic processes of lath bainite nucleation and growth by laser scanning confocal microscope in reheated weld metals, Metall. Mater. Trans. A. 48 (12) (2017) 5783–5798.

[29] J. Pak, D.W. Suh, H.K.D.H. Bhadeshia, Displacive phase transformation and surface effects associated with confocal laser scanning microscopy, Metall. Mater. Trans. A Phys. Metall. Mater. Sci. 43 (2012) 4520–4524, https://doi.org/10.1007/s11661-012-1264-8.

[30] R. Heard, J.E. Huber, C. Siviour, G. Edwards, E.d. Williamson-Brown, K. Dragnevski, An investigation into experimental in situ scanning electron microscope (SEM) imaging at high temperature, Rev. Sci. Instrum. 91 (6) (2020), https://doi.org/10.1063/1.5144981.

[31] J. Ma, J. Lu, L. Tang, J. Wang, L. Sang, Y. Zhang, Z. Zhang, A novel instrument for investigating the dynamic microstructure evolution of high temperature service materials up to 1150 °C in scanning electron microscope, Rev. Sci. Instrum. 91 (2020) 43704, https://doi.org/10.1063/1.5142807.

[32] J. Nutter, J. Qi, H. Farahani, W.M. Rainforth, S. van der Zwaag, van der Zwaag, In situ TEM Observations of the Growth of Bainitic Ferrite in an Fe-0.3 C-3Mn-1.5 Si-0.15 Mo Steel, Acta Mater. 252 (2023) 118924.

[33] V. Javaheri, N. Khodaie, A. Kaijalainen, D. Porter, Effect of niobium and phase transformation temperature on the microstructure and texture of a novel 0.40% C thermomechanically processed steel, Mater. Charact. 142 (2018) 295–308, https://doi.org/10.1016/j.matchar.2018.05.056.

[34] D.G. Lowe, Distinctive image features from scale-invariant keypoints, Int. J. Comput. Vis. 60 (2004) 91–110, https://doi.org/10.1023/B:VISI.0000029664.99615.94.

[35] A. Krull, T.O. Buchholz, F. Jug, Noise2void-Learning denoising from single noisy images, Proc. IEEE Comput. Soc. Conf. Comput. Vis. Pattern Recognit. (2019-June (2019)) 2124–2132, https://doi.org/10.1109/CVPR.2019.00223.

[36] H.K.D. Bhadeshia, bainite in steels, in: Bainite in Steels, 2001: p. 129,146.

[37] M. Pietrzyk, R. Kuziak, Modelling phase transformations in steel, Woodhead Publishing Limited, 2012. https://doi.org/10.1533/9780857096340.2.145.

[38] A. Pohjonen, Full Field Model Describing Phase Front Propagation, Transformation Strains, Chemical Partitioning, and Diffusion in Solid-Solid Phase Transformations, Adv. Theory Simulations. 2200771 (2023) 2200771, https://doi.org/10.1002/adts.202200771.

[39] A. Pohjonen, A. Kaijalainen, M. Somani, J. Larkiola, Analysis of bainite onset during cooling following prior deformation at different temperatures, Comput. Methods Mater. Sci. 17 (2017).

[40] E. Scheil, Anlaufzeit der Austenitumwandlung 8 (12) (1935) 565–567.

[41] V. Javaheri, S. Kolli, B. Grande, D. Porter, Insight into the induction hardening behavior of a new 0.40% C microalloyed steel: Effects of initial microstructure and thermal cycles, Mater. Charact. 149 (2019) 165–183, https://doi.org/10.1016/j.matchar.2019.01.029.

[42] R.L. Higginson, C.M. Sellars, Worked examples in quantitative metallography, 2003.